nature communications

Article

https://doi.org/10.1038/s41467-022-34924-z

Constraints on exotic spin-velocity-dependent interactions

Received: 29 March 2022

Accepted: 11 November 2022

Published online: 30 November 2022

Check for updates

Kai Wei[1,2,3], Wei Ji[4,5] ✉, Changbo Fu[6] ✉, Arne Wickenbrock[4,5], Victor V. Flambaum[5,7], Jiancheng Fang[1,2] & Dmitry Budker[4,5,8]

Experimental searches for exotic spin-dependent forces are attracting a lot of attention because they allow to test theoretical extensions to the standard model. Here, we report an experimental search for possible exotic spin-dependent force, specifically spin-and-velocity-dependent forces, by using a K-Rb-^{21}Ne co-magnetometer and a tungsten ring featuring a high nucleon density. Taking advantage of the high sensitivity of the co-magnetometer, the pseudomagnetic field from this exotic force is measured to be ≤7 aT. This sets limits on coupling constants for the neutron-nucleon and proton-nucleon interactions in the range of ≥0.1 m (mediator boson mass ≤2 μeV). The coupling constant limits are established to be $|g_V^n| \le 8.2\times10^{-11}$ and $|g_V^p| \le 3.7\times10^{-10}$, which are more than one order of magnitude tighter than astronomical and cosmological limits on the coupling between the new gauge boson such as Z′ and standard model particles.

Precision measurements are powerful tools to find new physics beyond the Standard Model. For example, the discrepancies revealed by the precision measurements of the muon anomalous magnetic moment[1,2] and the proton radius[3,4] have been analyzed as possible indications of "new" physics. Light particles, including the spin-1 boson Z′ and spin-0 Axion Like Particles (ALPs) were proposed to resolve these discrepancies[5,6], and are also promising candidates for dark matter[7–9]. If these particles exist, they mediate new long-range spin-dependent forces[10,11], and could be discovered in precision measurements.

Many experiments are conducted to search for long-range forces. Typical approaches include torsion pendulums[12], torsional oscillator[13], atomic magnetometers[14–17], nuclear magnetic resonance[18–21], nitrogen-vacancy (NV) centers in diamond[22], magnetic microscopes[23], polarized neutron experiments[24–26], and measurements of atomic and molecular electric dipole moments[27].

Mathematically, forces between two particles, which depend on velocity, spin, and distance, can be broken down into 15 terms of spin-dependent forces[10,11,28], which provides a guide on how to search them experimentally. Among the 15 terms, the spin-and-velocity-dependent (SVD) terms have received extensive attention in recent years[16,19,22,23,29]. Considering that these forces are mediated by Z′, the corresponding Lagrangian can be expressed as[11]

$$\mathcal{L}_{Z'} = Z'_\mu \sum_\psi \bar{\psi}\gamma^\mu (g_V + \gamma^5 g_A)\psi, \tag{1}$$

where ψ is the fermion field, γ^5 and γ^μ are Dirac matrices, and g_A and g_V are axial and vector coupling constants. One of the SVD potentials, V_{4+5}, as being noted in Ref. [10], can be derived from this Lagrangian[10,19],

$$V_{4+5} = \frac{-f_{4+5}\hbar^2}{8\pi mc}\left[(\hat{\boldsymbol{\sigma}}\cdot(\boldsymbol{v}\times\hat{\mathbf{r}})\right]\left(\frac{1}{\lambda r}+\frac{1}{r^2}\right)e^{-r/\lambda}, \tag{2}$$

where $f_{4+5} = -(g_A g_A + 3g_V g_V)/2$ is a dimensionless coupling factor, $\hbar$ is the reduced Planck constant, c is the speed of light, λ is the force range,

[1]School of Instrumentation Science and Opto-electronics Engineering, Beihang University, 100191 Beijing, China. [2]Hangzhou Extremely Weak Magnetic Field Major Science and Technology Infrastructure Research Institute, 310051 Hangzhou, China. [3]Hangzhou Innovation Institute, Beihang University, 310051 Hangzhou, China. [4]Helmholtz-Institut, GSI Helmholtzzentrum für Schwerionenforschung, Mainz 55128, Germany. [5]Johannes Gutenberg-Universität Mainz, Mainz 55128, Germany. [6]Key Lab of Nuclear Physics & Ion-beam Application (MoE), Institute of Modern Physics, Fudan University, 200433 Shanghai, China. [7]School of Physics, University of New South Wales, Sydney, NSW 2052, Australia. [8]Department of Physics, University of California, Berkeley, CA 94720-7300, USA. ✉e-mail: wei.ji.physics@gmail.com; cbfu@fudan.edu.cn

r and **v** are the relative distance and velocity between the two particles, $\hat{\sigma}$ is the spin of one fermion and m is its mass.

One can write V_{4+5} as $V_{4+5} = -\boldsymbol{\mu}\cdot\mathbf{B}_{\rm psd}$, where $\mathbf{B}_{\rm psd}$ is the pseudomagnetic field, and μ is the magnetic moment of the particle. Using bulk test material, the total pseudomagnetic field can be computed by integration over the volume of the material,

$$\mathbf{B}_{\rm psd} \equiv \frac{f_{4+5}\hbar^2}{8\pi mc\mu}\int \rho_N(\mathbf{r})(\boldsymbol{v}\times\hat{\mathbf{r}})\left(\frac{1}{\lambda r}+\frac{1}{r^2}\right)e^{-r/\lambda}d\mathbf{r}, \tag{3}$$

where $\rho_N(\mathbf{r})$ is the mass-source nucleon density at location **r** with the sensor chosen as the origin, where the "N" notes the average nucleon contribution to $\mathbf{B}_{\rm psd}$ from the mass-source nucleons which is a linear combination of the protons and neutrons in the material (for example, 74 protons and 110 neutrons for tungsten gives 74/184 proton and 110/184 neutron interaction constants). Accordingly, the exotic force decays exponentially with the relative distance and it is beneficial to use high-density test materials. In fact, non-magnetic materials, such as silica (nucleon density $1.33\times10^{24}\,\mathrm{cm}^{-3}$) and bismuth germanium oxide (BGO; nucleon density $4.3\times10^{24}\,\mathrm{cm}^{-3}$) are used as the test material in recent works[19,22]. Because the possible signals are expected to be weak, a high-sensitivity magnetometer like a Spin-Exchange Relaxation Free (SERF) device[30–33] is desired.

In this paper, we report a new measurement of V_{4+5} by using a K–Rb–^{21}Ne comagnetometer[34], and a tungsten test ring. Tungsten has a nucleon density of $1.15\times10^{25}\,\mathrm{cm}^{-3}$, which is among the highest-density practically-available non-magnetic materials. The sensitivity of SERF comagnetometers to pseudomagnetic fields acting on the sensor nuclei has been demonstrated to be better than $1\,\mathrm{fT/Hz^{1/2}}$[33,35], which is one order of magnitude more sensitive than the "spin-based amplifier" demonstrated recently[19]. With these advantages, limits on the V_{4+5} neutron-nucleon and proton-nucleon interactions have been achieved.

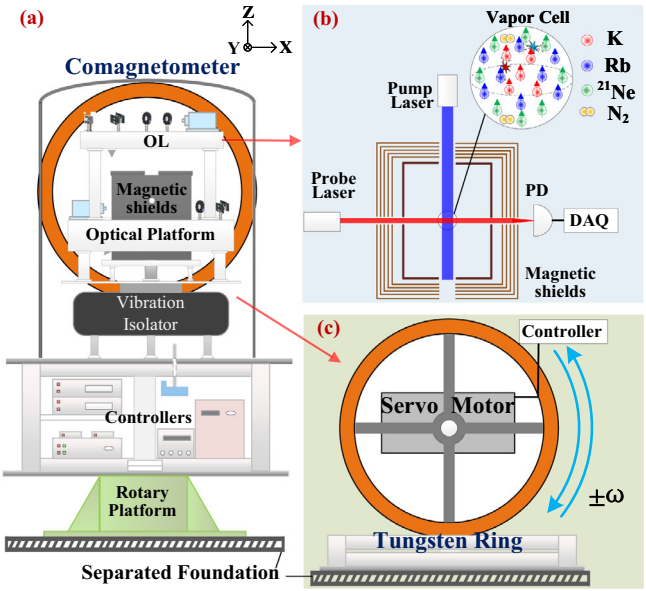

Fig. 1 | The experimental setup. a The structure of the whole equipment. The tungsten ring (nucleon source) is placed at the back of the comagnetometer along $\hat{y}$-axis. The center of the ring and the center of the comagnetometer cell are located at the same height. The comagnetometer is placed on a rotary platform that is isolated from the foundation of the tungsten ring. **b** The comagnetometer setup. The K, Rb, and ^{21}Ne atoms are spin-polarized along $\hat{z}$-axis (vertical) by the pump laser light. The transverse magnetic field can be measured with the probe laser light. The fluctuations of light intensities, frequencies, cell temperature are reduced with feedback. OL, optical elements and lasers. PD, photodetector. DAQ, data acquisition. The external magnetic field and magnetic noise are suppressed by shielding the vapor cell in a five-layer μ-metal shield and a ferrite shield. **c** The tungsten ring. The ring, with its duralumin support, is driven with a servo motor. It can rotate clockwise and counterclockwise.

Results

Experimental setup

The experimental setup is shown in Fig. 1. A tungsten–aluminum (W–Al) ring, composed of tungsten wires and its ring-shape duralumin support, serves as the nucleon source and is located behind a K–Rb–^{21}Ne comagnetometer. Driven with a servo motor, the W–Al ring can rotate clockwise or counterclockwise. The rotation axis of the ring is coaxial with the vapor cell along the $\hat{y}$ direction, along which the comagnetometer has the highest sensitivity. The angular position of the ring is monitored with a photoelectric encoder. If it exists, the pseudomagnetic field induced by the W–Al ring can be measured with the comagnetometer.

The K–Rb–^{21}Ne comagnetometer is similar to that of Refs. [35,36]. Hybrid optical pumping is utilized to improve the polarization homogeneity of alkali spins and hyperpolarization efficiency of noble-gas spins, where the optically thin K atoms are optically polarized with a circularly polarized K D1-line laser along the $\hat{z}$-axis and are used to polarize the optically thick Rb atoms via spin-exchange (SE) collisions between K and Rb atoms. With the help of Rb and K, the ^{21}Ne nucleus can be polarized through the spin-exchange-optical-pumping mechanism[37]. The precession of the Rb polarization is measured via optical rotation of a linearly polarized laser beam propagating along the $\hat{x}$-axis. The frequency of the laser is detuned from the Rb D1-line towards lower frequencies by about 240 GHz. Here the optically thick Rb ensemble is used for probing instead of the optically thin K ensemble, in order to improve the signal-to-noise ratio. The precession of the ^{21}Ne nuclei is probed with Rb atoms, and detected via optical rotation of the probe laser beam. The K–Rb–^{21}Ne comagnetometer is operated in the self-compensation regime to suppress magnetic noise. It is also operated in the SERF regime, which results in its high sensitivity to pseudomagnetic signals[32].

Principle

After zeroing the normal magnetic field, the leading terms in the comagnetometer signal in the self-compensation regime is given by[15]

$$S = K\frac{\gamma_e P_z^e}{R_{\rm tot}^e}\left(b_y^{\rm Ne} - b_y^e + \frac{\Omega_y}{\gamma_{\rm Ne}}\right), \tag{4}$$

where γ_e and $\gamma_{\rm Ne}$ are the gyromagnetic ratios of electrons and ^{21}Ne nuclei; P_z^e and $R_{\rm tot}^e$ are the equilibrium spin polarization and transverse spin relaxation rate of alkali atoms, respectively; K is a factor to transform the P_x^e to the output electric signal S; $b_y^{\rm Ne}$ and b_y^e are the exotic fields along the $\hat{y}$ axis that couple to ^{21}Ne and alkali atoms, Ω_y is the inertial rotation rate in $\hat{y}$ axis. Deploying in Eq.(4), we utilize the inertial rotation to calibrate the comagnetometer response to exotic fields, which is summarized by a s factor $\kappa_n \equiv K\gamma_e P_z^e/R_{\rm tot}^e$.

If we consider the specific coupling to fermions, the pseudomagnetic field on the ^{21}Ne nuclei can be written as

$$b_y^{\rm Ne} = B_p^n\zeta_n^{\rm Ne} + B_p^p\zeta_p^{\rm Ne}, \tag{5}$$

where $\zeta_n^{\rm Ne} = 0.58$ and $\zeta_p^{\rm Ne} = 0.04$ are the fraction factors for neutron and proton polarization in the ^{21}Ne nucleus, respectively[15,38], and B_p^p and B_p^n are the exotic fields acting on the proton and neutron, respectively. To detect $b_y^{\rm Ne}$, a quantum nondemolition approach is used. First, the precession of ^{21}Ne nuclear spin under the $b_y^{\rm Ne}$ is transferred to the Rb atoms through the Fermi-contact interaction. By measuring the precession of Rb atoms based on optical rotation, one can measure the $b_y^{\rm Ne}$.

https://doi.org/10.1038/s41467-022-34924-z

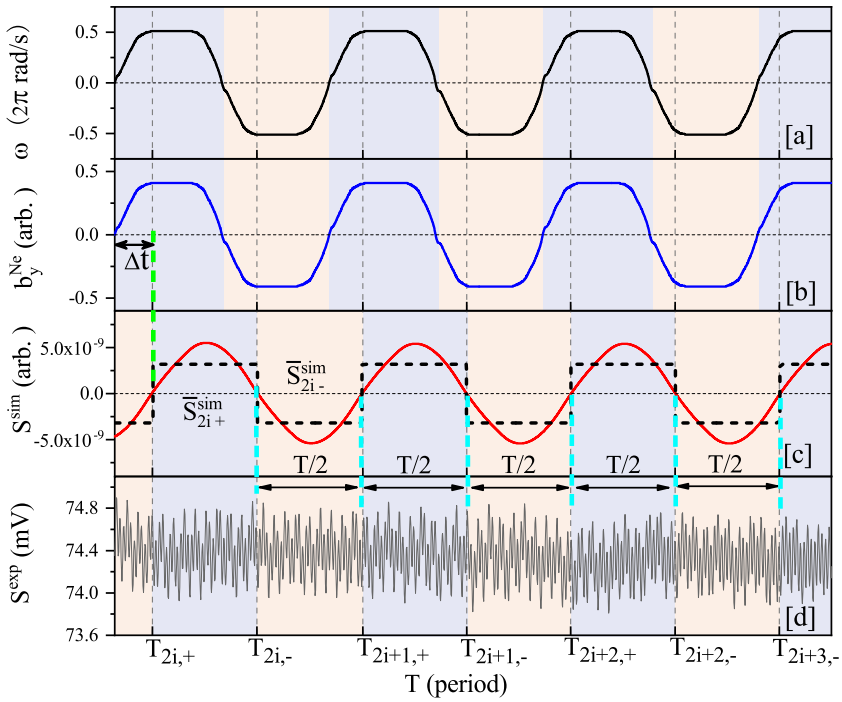

Fig. 2 | Data simulation and collection. a A representative measured angular velocity of the ring, $\omega(t)$. **b** The simulated pseudomagnetic field b_y^{Ne}. **c** The simulated response of the comagnetometer S^{sim}, which is delayed by Δt with respect to the b_y^{Ne}. The $\bar{S}^{sim}_{2i,+}$ and $\bar{S}^{sim}_{2i,-}$ are the average of each positive and negative half cycles, respectively. **d** The measured signal of the SERF comagnetometer.

Data taking and simulation

The signal from the comagnetometer, as well as the angular position of the ring, are recorded with a data-acquisition (DAQ) device. Data for an individual set are taken continuously for four hours, and 26 datasets are collected in total. Between the datasets the co-magnetometer performance is optimized. The parameters of the comagnetometer, including the cell temperature, laser power, laser frequency etc., are monitored and feedback controlled throughout the experiments to ensure its stability.

To optimize the sensitivity to the hypothetical force, it is modulated by modulating the rotation frequency of the tungsten ring. This way, the exotic signal is shifted into a frequency region with optimum noise performance of the co-magnetometer. The angular velocity of the ring ω^{exp} is measured with a high-precision photoelectric encoder and shown in Fig. 2a. The measured angular velocity is fitted with sinusoidal harmonics to obtain the amplitude (ω_{max} = 3.774 rad/s) and frequency (0.8369 Hz) of the fundamental harmonic.

The b_y^{Ne} induced by the test material can be simulated using Eq. (3) and Eq. (5). The major input parameters for the simulation are listed in Table 1, and the simulated b_y^{Ne} is shown in Fig. 2b. When calculating b_y^{Ne}, a coupling constant $f^{(0)}_{4+5}$ is assumed. In Fig. 2b, it is set to be $f^{(0)}_{4+5}$ = 1.

In Fig. 2c, the response of the comagnetometer S^{sim} is presented. This response signal is simulated based on Eq. (7) with parameters measured in the experiment. Because the main component of the b_y^{Ne} is at the fundamental harmonic and the bandwidth of the comagnetometer is narrow, the comagnetometer is mainly sensitive to the first harmonic component of b_y^{Ne}, which results in the approximately sinusoidal shape of S^{sim}. Compared with b_y^{Ne}, the S^{sim} has a phase shift $\Delta\phi = -67^\circ \pm 2^\circ$ due to the phase response of the comagnetometer (corresponding to a time delay of $\Delta t = 0.222 \pm 0.007$ s). In Fig. 2d, the corresponding experimental data S^{exp} are shown. There are slight beating patterns in the experimental data, which are due to the resonant vibrations of the isolation station and the table supporting the comagnetometer.

Table 1 | The experimental parameters and their error budget for the coupling coefficient

Parameter	Value	Δf^{exp}_{4+5} (×10⁻²¹)[a]
W–Al ring R (m)	0.475 ± 0.001	<0.001
Ring to cell center *X* (m)	0.478 ± 0.002	0.002
Ring to cell center *Y* (m)	0.000 ± 0.002	<0.001
Ring to cell center *Z* (m)	0.000 ± 0.002	<0.001
W–Al ring M (kg)	15.38 ± 0.05	0.001
ω_{max} (rad/s)	3.774 ± 0.001	<0.001
Calibrated κ_n (μV/fT)	1.67 ± 0.05	0.016
Modulation freq. (Hz)	0.8369 ± 0.0001	
Phase shift (deg)	−67° ± 2°	<0.001
Final f^{exp}_{4+5}	−0.54	±0.02 (syst.)
(λ = 10 m)		±1.62 (stat.)[b]

[a]The contribution to the error budget of f^n_{4+5} at λ = 10 m
[b]Error contribution from the uncertainties of the parameters listed above.

Limits on exotic forces

The coupling constant can be found by

$$f_{4+5} = f^{(0)}_{4+5}\frac{\bar{b}^{exp}}{\bar{b}^{sim}}, \quad (6)$$

where the $\bar{b}^{exp}$ and $\bar{b}^{sim}$ are exotic fields from the experiment and simulation respectively. The details of the data analysis can be found in the Supplementary Note 3.

A typical $\bar{S}^{exp}$ distribution, deduced from 4-hour data, is shown in the inset of Fig. 3. Note that the proton fraction of polarization in the Rb atom is $\zeta_p^{Rb} = 0.31$[39], but the Rb atoms' energy sensitivity is three orders of magnitude smaller than that of ^{21}Ne[15,40] (see the Supplementary Note 2B). Thus we only consider the proton spin in

https://doi.org/10.1038/s41467-022-34924-z

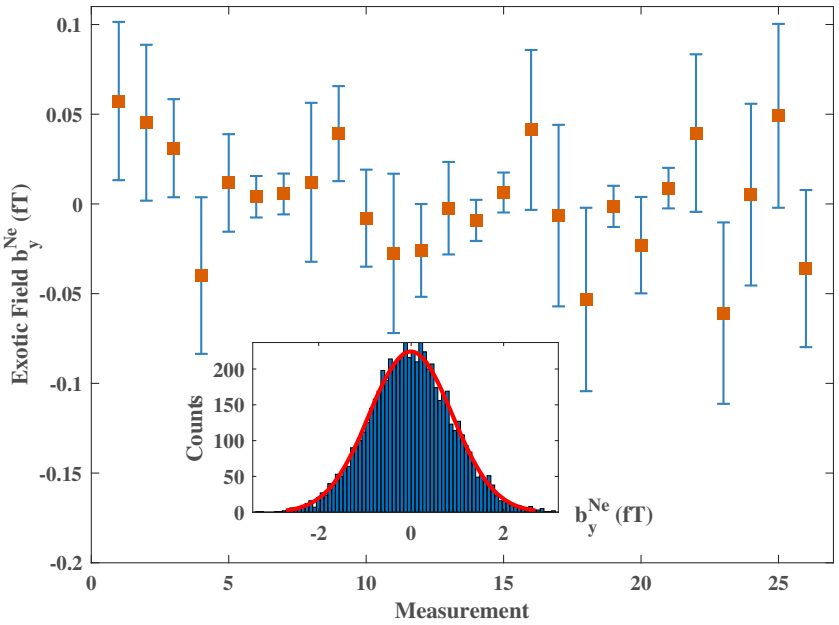

Fig. 3 | Experimental results of the b_y^{Ne}. Each point represents an average of a 4-h dataset, $\bar{b}_y^{Ne}$. The error bars represent the statistical and systematic error of the comagnetometer combined in quadrature. Histogram of $\bar{b}_y^{Ne}$ is shown in the inset, with the red curve being a Gaussian fit, and $\bar{\chi}^2 = 1.14$. The exotic field b_y^{Ne} is measured to be (2.4 ± 7.1)aT.

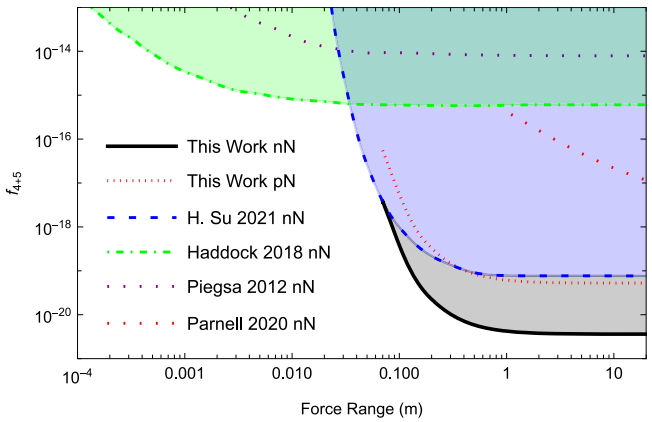

Fig. 4 | The experimental limits on f_{4+5}. The "n", "p", and "N" represent the neutron, proton, and average nucleon contribution respectively. The blue dashed line, "H.Su 2021", is from Ref. [19], the green dashed-dotted line, "Haddock 2018", is from Ref. [24], the yellow dotted line, "Piegsa 2012", is from Ref. [25], the red dashed line, "Parnell 2020", is from Ref. [50]. The black solid line and red dotted line represent our new results for "nN" and "pN" respectively.

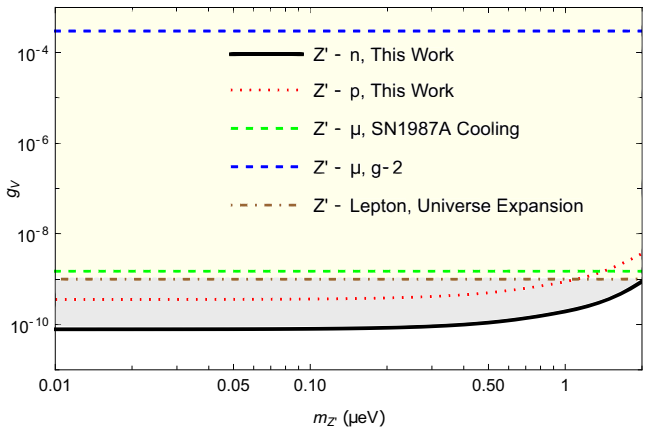

Fig. 5 | The experimental limits on the vector coupling constant g_V of the Z' particle. The black solid line and red dotted line are set by this work by searching for the exotic spin-dependent force. The blue dashed line is set by the $g-2$ experiment[41,44,45], the brown dotted-dashed line is set by the neutrino production in the expansion of the early universe[41], the green dashed line, is from the analysis of the supernova SN1987 cooling[44]. The shaded areas are the parameter space excluded by the corresponding experiments.

^{21}Ne and ignore that in Rb atoms. Using all the 104-hour data, the pseudomagnetic field b_y^{Ne} is measured to be (2.4 ± 7.1)aT. This results in new limits on the dimensionless coupling factor of the new force $|f_{4+5}| \le 3.4 \times 10^{-21}$ with 95% confidence level at the force range of 10 m. The limits on the coupling between the source nucleon with the ^{21}Ne neutron and proton are set to be $|f^n_{4+5}| = |f_{4+5}|/\zeta_n^{Ne} \le 5.9 \times 10^{-21}$ and $|f^p_{4+5}| = |f_{4+5}|/\zeta_p^{Ne} \le 8.5 \times 10^{-20}$ respectively. Our experiment results and a comparison with the results in the literature are shown in Fig. 4. Our result on the coupling with neutron is more than an order of magnitude better than that of previous works. The limits on exotic coupling with proton is set by this work for the first time to the best of our knowledge. For the coupling to electron spins, our experimental result is comparable to that of a recent work in Ref. [29].

It may be useful to consider specific cases for coupling, using the fact that $f_{4+5} = \frac{1}{2} g_A g_A - \frac{3}{2} g_V g_V$. Assuming $g_A g_A = 0$, we have $|(\zeta_p^{Ne} g_V^p + \zeta_n^{Ne} g_V^n)(\zeta_p^W g_V^p + \zeta_n^W g_V^n)| \le 2.3 \times 10^{-21}$, where $\zeta_n^W = 0.588$ and $\zeta_p^W = 0.412$ are the neutron and proton mass contribution in the W–Al mass source. If we assume $g_V^p = 0$, we get a limit on $|g_V^n| \le 8.2 \times 10^{-11}$. Conversely, if we assume $g_V^n = 0$, we get $|g_V^p| \le 3.7 \times 10^{-10}$. The coupling limit $|g_A^p| \le 6.4 \times 10^{-10}$ and $|g_A^n| \le 1.4 \times 10^{-10}$ is also set using the same method.

A comparison of the limits on g_V, the vector coupling constant between Z′ and standard model particles, between this SVD force result and other results including the cosmology and astronomy is shown in Fig. 5. The 'Z'-Lepton Universe Expansion' line is excluded by

https://doi.org/10.1038/s41467-022-34924-z

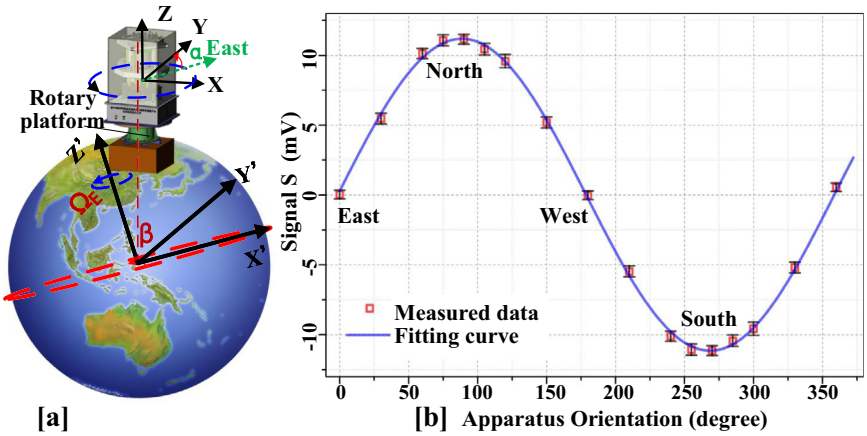

Fig. 6 | Calibration of the comagnetometer. a The comagnetometer is rotated by a rotary platform. The sensitive axis ($\hat{y}$) of comagnetometer is directed along different direction. Hence, the projection of Earth rotation along $\hat{y}$ can be used to calibrate the comagnetometer. β is the latitude of the lab, α is the orientation angle of $\hat{y}$ with respect to the east direction in the horizontal plane. **b** The measured dots at different direction are fitted by a sinusoidal function. The error bars represent statistical errors (standard deviations).

the effective number of neutrino species $\Delta N_{\rm nef} \approx 0.2$ in the early universe[41]. The authors of this work assume that Z′ can decay to neutrinos and affect the expansion of the universe. This model can relax the 3σ tension of Hubble constants, i.e., the discrepancy between local measurements and temperature anisotropies of the cosmic microwave background[41–43]. The 'Z'-μ, $g-2$' is excluded by the muon g−2 experiment[41,44,45]. Note that the anomalous magnetic moment of muon can also be used to search for the spin-0 boson, such as axion like particles[6]. The 'Z'-μ, SN1987A Cooling' is excluded by the supernova SN1987A, assuming the new gauge boson Z′ decreases the cooling time[44]. Our results represent more than one order of magnitude tighter constraints than previous ones.

Discussion

The main advantage of this experiment compared to that in Ref. [19] are attributed to the high nucleon density of the nucleon source and the ultrahigh sensitivity of the comagnetometer. Tungsten has nucleon density approximately four times that of BGO, and our comagnetometer sensitivity is approximately one order of magnitude better than the ^{129}Xe based magnetometer used in Ref. [19].

The comagnetometer can also be used to search for many terms of spin-spin-velocity-dependent forces if one can use a spin-polarized source, such as a pure-iron shielded $SmCo_5$ electron-spin source[14]. For four terms of the spin-spin-velocity-dependent forces, new limits on electron-neutron and electron-proton interaction can be set in the force range ≥1 cm[46], which would complement the results of[47] for interaction ranges exceeding 1 km.

The techniques used in this work can be used to search for a broad class of beyond-standard-model particles[10,11,28]. The search for such particles is motivated, among other things, by the attempt to understand the composition of the dark sector (dark matter and dark energy). However, similar to other spin-dependent force searches, it does not, in any way, rely on specific local dark-sector properties, e.g., the local dark-matter density. If the exotic-force mediator is a Z′-boson, the interactions could violate parity, however, the current experiment does not exploit parity-violating effects. Indeed, the interaction in Eq. (2) is P- and T-even.

In conclusion, in this work, we have searched for exotic spin- and velocity-dependent interactions and, for the force range larger than several centimeters, improved the limits on the mass interactions with neutrons by more than an order of magnitude, while also setting a stringent limit on mass interactions with protons. This result demonstrates that the spin-dependent force approach is competitive in terms of sensitivity to new bosons with the cosmological and astronomical searches. Z′ can also be searched through pseudovector parity-violation couplings [47,48].

Methods

Calibration

The Earth rotation speed $\Omega_E = 7.292 \times 10^{-5}$ rad/s is used to calibrate the system. Mounted on a precision rotary platform, the apparatus can rotate in the horizontal plane as shown in Fig. 6 [a]. The Ω_y in Eq. (4) can be written as $\Omega_y = \Omega_E^h \sin(\alpha)$, where $\Omega_E^h = \Omega_E \cos(\beta)$ is the projection of $\mathbf{\Omega}_E$ in the horizontal plane, $\beta = 39.983^{\circ}$ is the latitude of the laboratory, and α is the relative azimuth angle of the sensitive $\hat{y}$ axis of the comagnetometer. Therefore, by fitting the measured signals with $S(\alpha) = \kappa_n \Omega_E^h \sin(\alpha)/\gamma_n$, the calibration factor κ_n can be obtained. As shown in Fig. 6 [b], the calibration factor at this near-DC frequency is measured to be κ_n(DC)=$(4.18 \pm 0.07) \times 10^{-6}$ V/fT with the $\bar{\chi}^2 = 0.687$.

In the self-compensation comagnetometer, the frequency responses to normal magnetic fields, inertial rotations ($B_{x/y}$, and $\Omega_{x/y}$) and exotic fields ($b_y^{\rm Ne}$ and b_y^e) are determined by four parameters, which are the Fermi-contact-interaction fields between noble-gas atoms and alkali atoms ($\lambda M_0^e P_z^e$ and $\lambda M_0^n P_z^n$)[49], and the transverse relaxation rates ($1/T_{2e}$ and $1/T_{2n}$). These four parameters are independently measured to be (110.6 ± 2.2) nT, (579.4 ± 2.1) nT, $(3.7 \pm 0.4) \times 10^3$ /s, and (0.063 ± 0.007) /s, respectively[36]. Particularly, the noble-gas nuclear spins and alkali electron spins are strongly coupled around the self-compensation point, such that the damping rate of nuclear spins is sped up by electron spins, while electron spins are slowed down[36]. The damping rate of nuclear spins is measured to be $2\pi \times (0.907 \pm 0.006)$/s by fitting the damping oscillation response to step magnetic field excitation, which is significantly larger than the $1/T_{2n}$ owing to the coupling between nuclear spins and electron spins. More details about the analysis of the comagnetometer can be found in Supplementary Note 2 and 3.

Simulation

The spin dynamics of the comagnetometer could be described by the coupled Bloch equations[32,36]:

$$\begin{aligned}\frac{\partial \mathbf{P}^e}{\partial t} = & \frac{\gamma_e}{Q}\left(\mathbf{B} + \lambda M_0^n \mathbf{P}^n + \mathbf{b}^e + \mathbf{\Omega}\frac{Q}{\gamma_e}\right) \times \mathbf{P}^e \\ & + \frac{P_{z0}^e \hat{z} - \mathbf{P}^e}{Q\{T_{1e}, T_{2e}, T_{2e}\}}, \\ \frac{\partial \mathbf{P}^n}{\partial t} = & \gamma_{\rm Ne}\left(\mathbf{B} + \lambda M_0^e \mathbf{P}^e + \mathbf{b}^{\rm Ne} + \frac{\mathbf{\Omega}}{\gamma_{\rm Ne}}\right) \times \mathbf{P}^{\mathbf{n}} \\ & + \frac{P_{z0}^n \hat{z} - \mathbf{P}^n}{\{T_{1n}, T_{2n}, T_{2n}\}},\end{aligned} \tag{7}$$

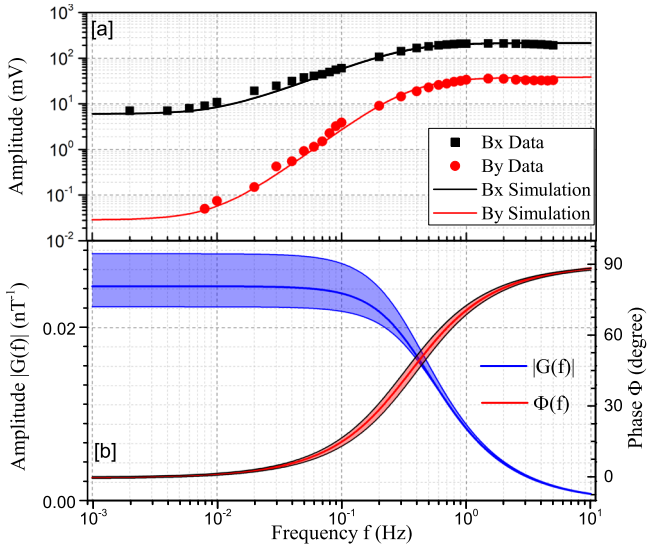

Fig. 7 | Frequency responses of the comagnetometer. a A comparison of the measured frequency responses to normal magnetic field and the simulated results. The simulated results are calculated with Eq.(7) based on measured parameters ($\lambda M_0^e \mathbf{P}_z^e$, $\lambda M_0^n \mathbf{P}_z^n$, T_{2e} and T_{2n}) with only one free parameter to describe the scale. The measured data agree well with the simulation of the Bloch equation Eq. (7), which confirms the validity of the simulation. **b** The simulated amplitude-frequency response (blue) and phase-frequency response (red) to exotic field b_y^{Ne}. The uncertainty bands of the phase and amplitude are calculated based on the uncertainties of the measured parameter.

where Q is the slowing-down factor arising from spin-exchange collisions and hyperfine interaction, $\mathbf{P^e}$ and $\mathbf{P^n}$ are the spin polarizations of alkali electron and ^{21}Ne nuclear, respectively. $\mathbf{B}$ and $\mathbf{\Omega}$ are external magnetic field and inertial rotation. The Fermi-contact interaction between alkali atoms and ^{21}Ne atoms can be described by an effective magnetic field $\lambda M_0^{e,n}\mathbf{P}^{e,n}$, where M_0^n (M_0^e) is the maximum magnetization of ^{21}Ne nucleon (alkali electron)[49]. For a uniformly spin-polarized spherical cell, $\lambda = 8\pi\kappa_0/3$, where κ_0 is the enhancement factor. T_{1e} and T_{2e} are the longitudinal and transverse relaxation rates for alkali electron spin, respectively, and T_{1n} and T_{2n} are the longitudinal and transverse relaxation times for the ^{21}Ne nucleon spin.

As shown in Fig. 7 [a], to further verify the validity of the parameters $\lambda M_0^e P_z^e$, $\lambda M_0^n P_z^n$, T_{2e}, and T_{2n}) and the frequency response model, the frequency responses to B_y and B_x are measured and compared with the simulated results with Eq. (7) based on these four parameters with only one free parameter to describe the scale. The measured signals are consistent with the simulated results. Therefore, the response of the comagnetometer S^{sim} to the exotic field b_y^{Ne} can be simulated by solving the Bloch Eqs. (7)[40] with these verified parameters. The simulation result of the amplitude and phase response to b_y^{Ne} is shown in Fig. 7 [b]. The results are further used to correct the calibration factor κ_n and the phase retardation $\Delta\phi$. For the modulation frequency at 0.83681(1) Hz, the amplitude response is 0.40 ± 0.01 of that in DC. Meanwhile, the phase shift $\Delta\phi$ is $-67^\circ \pm 2^\circ$. The corrected calibration factor is $\kappa_n(0.84\,\text{Hz}) = (1.67 \pm 0.05) \times 10^{-6}$ V/fT. A detailed analysis of the uncertainty of calibration factor can be found in Supplementary Note 3.

Data availability

The datasets generated during the current study are available from the corresponding author on request.

References

1. Abi, B. et al. Measurement of the positive muon anomalous magnetic moment to 0.46 ppm. *Phys. Rev. Lett.* **126**, 141801 (2021).
2. Bennett, G. W. et al. Final report of the e821 muon anomalous magnetic moment measurement at bnl. *Phys. Rev. D* **73**, 072003 (2006).
3. Karr, J.-P. & Marchand, D. Progress on the proton-radius puzzle. *Nature* **575**, 61–62 (2019).
4. Xiong, W. et al. A small proton charge radius from an electron–proton scattering experiment. *Nature* **575**, 147–150 (2019).
5. Heeck, J. Lepton flavor violation with light vector bosons. *Phys. Lett. B* **758**, 101–105 (2016).
6. Yan, H. et al. Constraining exotic spin dependent interactions of muons and electrons. *Eur. Phys. J. C* **79**, 1–5 (2019).
7. Okada, N., Okada, S., Raut, D. & Shafi, Q. Dark matter $z\prime$ and xenon1t excess from $u(1)x$ extended standard model. *Phys. Lett. B* **810**, 135785 (2020).
8. Athron, P. et al. Global fits of axion-like particles to xenon1t and astrophysical data. *J. High Energy Phys.* **2021**, 1–40 (2021).
9. Co, R. T., Hall, L. J. & Harigaya, K. Predictions for axion couplings from alp cogenesis. *J. High Energy Phys.* **2021**, 1–23 (2021).
10. Dobrescu, B. A. & Mocioiu, I. Spin-dependent macroscopic forces from new particle exchange. *J. High Energy Phys.* **11**, 005 (2006).
11. Fadeev, P. et al. Revisiting spin-dependent forces mediated by new bosons: potentials in the coordinate-space representation for macroscopic- and atomic-scale experiments. *Phys. Rev. A* **022113**, 1–7 (2019).
12. Terrano, W., Adelberger, E., Lee, J. & Heckel, B. Short-range, spin-dependent interactions of electrons: a probe for exotic pseudo-goldstone bosons. *Phys. Rev. Lett.* **115**, 201801 (2015).
13. Aldaihan, S., Krause, D., Long, J. & Snow, W. Calculations of the dominant long-range, spin-independent contributions to the interaction energy between two nonrelativistic Dirac fermions from double-boson exchange of spin-0 and spin-1 bosons with spin-dependent couplings. *Phys. Rev. D* **95**, 096005 (2017).
14. Ji, W. et al. New experimental limits on exotic spin-spin-velocity-dependent interactions by using SmCo 5 spin sources. *Phys. Rev. Lett.* **121**, 261803 (2018).
15. Almasi, A., Lee, J., Winarto, H., Smiciklas, M. & Romalis, M. V. New limits on anomalous spin-spin interactions. *Phys. Rev. Lett.* **125**, 201802 (2020).
16. Kim, Y. J., Chu, P.-H. & Savukov, I. Experimental constraint on an exotic spin-and velocity-dependent interaction in the sub-mev range of axion mass with a spin-exchange relaxation-free magnetometer. *Phys. Rev. Lett.* **121**, 091802 (2018).
17. Hunter, L. & Ang, D. Using geoelectrons to search for velocity-dependent spin-spin interactions. *Phys. Rev. Lett.* **112**, 091803 (2014).
18. Tullney, K. et al. Constraints on spin-dependent short-range interaction between nucleons. *Phys. Rev. Lett.* **111**, 100801 (2013).
19. Su, H. et al. Search for exotic spin-dependent interactions with a spin-based amplifier. *Sci. Adv.* **7**, eabi9535 (2021).
20. Arvanitaki, A. & Geraci, A. A. Resonantly detecting axion-mediated forces with nuclear magnetic resonance. *Phys. Rev. Lett.* **113**, 161801 (2014).
21. Ledbetter, M., Romalis, M. V. & Kimball, D. J. Constraints on short-range spin-dependent interactions from scalar spin-spin coupling in deuterated molecular hydrogen. *Phys. Rev. Lett.* **110**, 040402 (2013).
22. Jiao, M., Guo, M., Rong, X., Cai, Y.-F. & Du, J. Experimental constraint on an exotic parity-odd spin-and velocity-dependent interaction with a single electron spin quantum sensor. *Phys. Rev. Lett.* **127**, 010501 (2021).
23. Ren, X. et al. Search for an exotic parity-odd spin-and velocity-dependent interaction using a magnetic force microscope. *Phys. Rev. D* **104**, 032008 (2021).
24. Haddock, C. et al. A search for possible long range spin dependent interactions of the neutron from exotic vector boson exchange. *Phys. Lett. B* **783**, 227–233 (2018).

25. Piegsa, F. M. & Pignol, G. Limits on the axial coupling constant of new light bosons. *Phys. Rev. Lett.* **108**, 181801 (2012).
26. Yan, H. & Snow, W. New limit on possible long-range parity-odd interactions of the neutron from neutron-spin rotation in liquid he 4. *Phys. Rev. Lett.* **110**, 082003 (2013).
27. Stadnik, Y., Dzuba, V. & Flambaum, V. Improved limits on axionlike-particle-mediated p, t-violating interactions between electrons and nucleons from electric dipole moments of atoms and molecules. *Phys. Rev. Lett.* **120**, 013202 (2018).
28. Moody, J. & Wilczek, F. New macroscopic forces? *Phys. Rev. D* **30**, 130 (1984).
29. Wu, K. et al. Experimental limits on exotic spin and velocity dependent interactions using rotationally modulated source masses and an atomic-magnetometer array. *Phys. Rev. Lett.* **129**, 051802 (2022).
30. Allred, J., Lyman, R., Kornack, T. & Romalis, M. V. High-sensitivity atomic magnetometer unaffected by spin-exchange relaxation. *Phys. Rev. Lett.* **89**, 130801 (2002).
31. Kominis, I., Kornack, T., Allred, J. & Romalis, M. V. A subfemtotesla multichannel atomic magnetometer. *Nature* **422**, 596–599 (2003).
32. Kornack, T., Ghosh, R. & Romalis, M. Nuclear spin gyroscope based on an atomic comagnetometer. *Phys. Rev. Lett.* **95**, 230801 (2005).
33. Vasilakis, G., Brown, J., Kornack, T. & Romalis, M. Limits on new long range nuclear spin-dependent forces set with a k- he 3 comagnetometer. *Phys. Rev. Lett.* **103**, 261801 (2009).
34. Quan, W., Wei, K., Zhao, T., Li, H. & Zhai, Y. Synchronous measurement of inertial rotation and magnetic field using a K-Rb-Ne 21 comagnetometer. *Phys. Rev. A* **100**, 012118 (2019).
35. Chen, Y. et al. Spin exchange broadening of magnetic resonance lines in a high-sensitivity rotating K-Rb-21Ne co-magnetometer. *Sci. Rep.* **6**, 1–12 (2016).
36. Wei, K. et al. Simultaneous determination of the spin polarizations of noble-gas and alkali-metal atoms based on the dynamics of the spin ensembles. *Phys. Rev. Appl.* **13**, 044027 (2020).
37. Walker, T. G. & Happer, W. Spin-exchange optical pumping of noble-gas nuclei. *Rev. Mod. Phys.* **69**, 629 (1997).
38. Brown, B., Bertsch, G., Robledo, L., Romalis, M. V. & Zelevinsky, V. Nuclear matrix elements for tests of local lorentz invariance violation. *Phys. Rev. Lett.* **119**, 192504 (2017).
39. Kimball, D. J. Nuclear spin content and constraints on exotic spin-dependent couplings. *New J. Phys.* **17**, 073008 (2015).
40. Padniuk, M. et al. Response of atomic spin-based sensors to magnetic and nonmagnetic perturbations. *Sci. Rep.* **12**, 1–9 (2022).
41. Escudero, M., Hooper, D., Krnjaic, G. & Pierre, M. Cosmology with a very light lμ-lτ gauge boson. *J. High Energy Phys.* **2019**, 1–29 (2019).
42. Aghanim, N. et al. Erratum: Planck 2018 results: VI. Cosmological parameters. *Astron. Astrophys.* **652**, C4 (2021).
43. Riess, A. G. et al. Milky way cepheid standards for measuring cosmic distances and application to gaia dr2: implications for the hubble constant. *Astrophys. J.* **861**, 126 (2018).
44. Croon, D., Elor, G., Leane, R. K. & McDermott, S. D. Supernova muons: new constraints on z' bosons, axions and alps. *J. High Energy Phys.* **2021**, 1–28 (2021).
45. Tanabashi, M. et al. Review of particle physics. *Phys. Rev. D* **98**, 030001 (2018).
46. Ji, W., Fu, C. & Gao, H. Searching for new spin-dependent interactions with smco5 spin sources and a spin-exchange-relaxation-free comagnetometer. *Phys. Rev. D* **95**, 075014 (2017).
47. Antypas, D. et al. Isotopic variation of parity violation in atomic ytterbium. *Nat. Phys.* **15**, 120–123 (2019).
48. Fadeev, P., Ficek, F., Kozlov, M. G., Budker, D. & Flambaum, V. V. Pseudovector and pseudoscalar spin-dependent interactions in atoms. *Phys. Rev. A* **105**, 022812 (2022).
49. Romalis, M. & Cates, G. Accurate 3 he polarimetry using the Rb Zeeman frequency shift due to the Rb-3 he spin-exchange collisions. *Phys. Rev. A* **58**, 3004 (1998).
50. Parnell, S. et al. Search for exotic spin-dependent couplings of the neutron with matter using spin-echo based neutron interferometry. *Phys. Rev. D* **101**, 122002 (2020).

Acknowledgements

The authors thank Xing Heng and Zitong Xu for debugging and operating the servo motor. This work is supported by the National Natural Science Foundation of China (NSFC) under Grant Nos. 61925301 for Distinguished Young Scholars, 11875191(CF), and 12235003(CF), the China postdoctoral Science Foundation (Grant No. 2021M700345), the DFG Project ID 390831469: EXC 2118 (PRISMA+ Cluster of Excellence), by the German Federal Ministry of Education and Research (BMBF) within the Quantumtechnologien program (Grant No. 13N15064). and by the QuantERA project LEMAQUME (DFG Project Number 500314265).

Author contributions

K.W., W.J., C.B.F, J.C.F., and D.B. proposed this study. K.W. and W.J. performed the experiment and analyzed the data. K.W., W.J., C.B.F., A.W., V.F., and D.B. wrote the manuscript.

Competing interests

The authors declare no competing interests.

Additional information

Supplementary information The online version contains supplementary material available at https://doi.org/10.1038/s41467-022-34924-z.

Correspondence and requests for materials should be addressed to Wei Ji or Changbo Fu.

Peer review information *Nature Communications* thanks the anonymous reviewer(s) for their contribution to the peer review of this work.